Heliyon 8 (2022) e12566

Contents lists available at ScienceDirect

Heliyon

journal homepage: www.cell.com/heliyon

Research article

Structure, luminescence properties and energy transfer of terbium and samarium co-doped barium based apatite phosphor with tunable emission colour

Kun Nie [a,b,*], Ranran Zhou [a], Chi-An Cheng [c], Xiuqiang Duan [a], Ziyao Hu [a], Lefu Mei [d], Haikun Liu [e], Yuanyuan Zhang [e], Luoxin Wang [a], Hua Wang [a], Xiaoxue Ma [a,**]

[a] State Key Laboratory of New Textile Materials & Advanced Processing Technology, Hubei Key Laboratory for New Textile Materials and Applications, School of Materials Science and Engineering,Wuhan Textile University, Wuhan, 430200, PR China
[b] Key Laboratory of Testing and Tracing of Rare Earth Products for State Market Regulation, Jiangxi University of Science and Technology, Ganzhou, 341000, PR China
[c] Department of Bioengineering, University of California Los Angeles, Los Angeles 90095, CA, USA
[d] Beijing Key Laboratory of Materials Utilization of Nonmetallic Minerals and Solid Wastes, National Laboratory of Mineral Materials, School of Materials Sciences and Technology, China University of Geosciences(Beijing), Beijing 100083, PR China
[e] Department of Energy and Chemical Engineering, Dongguan University of Technology, Dongguan 523808, PR China

HIGHLIGHTS

- $Ba_2La_{2.85-x}(SiO_4)_3F:0.15Tb^{3+},xSm^{3+}$ phosphors were prepared for the first time.
- Energy transfer mechanism from Tb^{3+} to Sm^{3+} is quadrupole-quadrupole interaction.
- The color of phosphors could be adjusted from green, yellow to reddish colour.

GRAPHICAL ABSTRACT

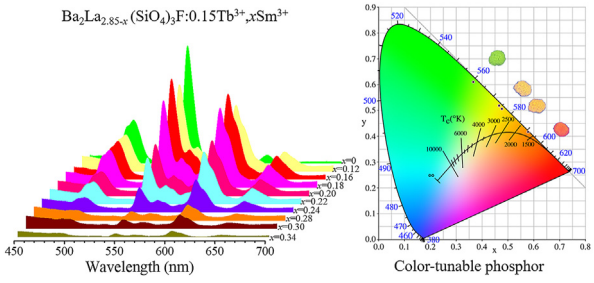

ARTICLE INFO

Keywords:
Rare earth
Photoluminescence
High-temperature solid-state method
Rare earth doped phosphor
Luminescence property

ABSTRACT

$Ba_2La_{2.85-x}Tb_{0.15}Sm_x(SiO_4)_3F$ (BLSOF:$0.15Tb^{3+},xSm^{3+}$) is a polychromatic phosphor with an apatite structure that was manufactured through a solid-state process. X-ray diffraction (XRD) and a scanning electron microscope (SEM) were utilized to examine the phosphor's phase and morphology. Using the Rietveld technique, the as-prepared phosphor structure was validated. By progressively raising the doping contents of the samarium, the phosphors emitted multicoloured luminescence from short to long wavelengths as indicated by analysis of the optical performance. Overall, the data provide strong evidence that the transfer of energy in BLSOF:$0.15Tb^{3+},xSm^{3+}$ is responsible for the phosphor's colour-tunable property.

* Corresponding author.
** Corresponding author.
E-mail addresses: knie@wtu.edu.cn (K. Nie), maxiaoxue2010@126.com (X. Ma).

https://doi.org/10.1016/j.heliyon.2022.e12566
Received 21 October 2022; Received in revised form 10 November 2022; Accepted 15 December 2022

1. Introduction

Due to their extraordinary and distinctive properties, light-emitting diodes (LEDs) are often regarded as representing the fourth generation of lighting sources in the general lighting market [1, 2, 3]. Attractive colours, tiny size, and exquisite construction all contribute to LEDs' popularity for use in decorating and illuminating urban areas [4, 5, 6]. One strategy for enabling LEDs to produce practical colours in their illuminance was to combine phosphors with n-UV chips, which emit light in the range of 350–420 nm [7, 8, 9]. To clarify more specifically, the phosphor consists of activators and hosts (there are a few cases in which sensitizers are incorporated) [10]. Recently, single-phase multicolour phosphors have preferentially recorded great improvement owing to the revelation that they can avoid various lighting limitations, including varying light decay durations and other issues. The ion pairs Tb^{3+}→Sm^{3+} can create a light of multiple colours, which would be beneficial to meet our requirements. When used in phosphor activation processes, samarium is capable of producing red light, in contrast, terbium may be employed as a phosphor sensitizer to produce green light [11, 12, 13]. Apatite compound is frequently selected as the host owing to its great chemical stability that is unaltered by the fluctuating crystal field environment. The structural component of apatite has the chemical formula $M_{10}(XO_4)_6Y_2$. Depending on its valence, M could be a monovalent cation like an alkali metal, a divalent cation like an alkaline earth metal, or a trivalent cation like a lanthanide element; X represents P, Si, Ge, S, etc; Y typically represents either halogen or oxygen, each of which performs the role of a channel anion [14, 15, 16]. Apatite compounds, such as $Sr_9Gd(PO_4)_5(SiO_4)F_2$ [17], $Ba_2La_3(SiO_4)_3F$ [18], and $Ba_2La_3(SiO_4)_3Cl$ [19], have been used in various research fields. Given that a range of single-phase multicolour phosphors could be produced by transferring energy among rare earth ions, structural control makes it possible to produce a large number of variations that can be derived from the crystalline structure of apatite, which may greatly expand the variety of light-emitting materials and offer new alternatives for the solid-state lighting sector. In our previous paper, we studied the luminous properties and energy transfer of $Ba_2La_{2.85-x}Tb_{0.15}Eu_x(SiO_4)_3F$ [18] and $Sr_2La_3(SiO_4)_3F$:Tb^{3+},Sm^{3+} [20]. Nevertheless, research on terbium and samarium-doped $Ba_2La_3(SiO_4)_3F$ (BLSOF) is lacking, as far as we can tell.

To examine its structure and luminous features, particularly its energy transfer, we prepared the Tb^{3+}→Sm^{3+} doped with $Ba_2La_3(SiO_4)_3F$ phosphor, which exhibits an apatite structure. By steadily altering the doping concentration of rare earth ions while keeping the host compound undisturbed, green, yellow, and reddish tunable phosphors were created. Phosphors were also analyzed for their morphology and spectrum characteristics. A greater comprehension of this single phase and multicolour phosphor might help expand the solid-state lighting knowledge base, which has profound implications in theory and practice.

2. Experimental details

2.1. Samples synthesis

A standard solid-state method was used at high temperatures to synthesize BLSOF:0.15Tb^{3+},xSm^{3+} phosphors. Throughout the experiment, we did not use the reducing atmosphere. The necessary chemicals are as follows: analytical grade $BaCO_3$, SiO_2, NH_4HF_2, and remarkably pure La_2O_3 (99.99%), Tb_4O_7 (99.99%), and Sm_2O_3 (99.99%). The chemicals used in the experiment were purchased from Zhengzhou Feynman Biotechnology Co., Ltd (Zhengzhou, China, mall.shiyanjia.com). The chosen compounds were weighted corresponding to their stoichiometric ratio (0.0001 g accuracy). These chemicals had not been subjected to treatment in any way before or during the weighing process. Afterwards, these compounds were mixed and subjected to thorough grinding in a single mortar. Subsequently, a corundum crucible containing the homogenous mixture was put into a high-temperature tube furnace and heated for 5h at 1350 °C before being left to cool to room temperature (RT). In preparation for subsequent structural and spectral tests, the sintered block was powdered by grinding.

2.2. Measurement

2.2.1. Structure and morphology

The diffraction data were gathered utilizing a D8 high-resolution X-ray diffractometer operated on 40 kV and 30 mA Cu-K radiation (λ = 0.15406 nm, $2\theta = 10°–80°$, Bruker, Germany). Depending on the X-ray diffraction (XRD) results, the powder form crystalline configuration was refined via a step scan at a speed of 0.02°/step. Each step lasted for a total of 3 s, and a range of 5°–130° was scanned in 2θ. By employing Topas 3.0's refining procedure, the crystallographic information file (CIF) was obtained. A Hitachi scanning electron microscope (SEM), model number JSM-6701F, made in Japan, was utilized to investigate the microscopic characteristics.

2.2.2. Spectra

The luminescent spectrum was measured at RT with a Hitachi F-4700 fluorescence spectrophotometer. This device was fitted with a xenon light with a power output of 150 W and 400 V. The luminous sample was placed in the sample cell of the spectrometer, and then a specific excitation wavelength was designated to irradiate the sample, to obtain the photoluminescence emission (PL) spectrum of the sample. Similarly, the sample was placed in the sample cell of the spectrometer, and then a specific emission wavelength was designated to monitor the photoluminescence excitation (PLE) spectrum of the sample. The sample's fluorescent lifetime of the samples was determined with the assistance of the Edinburgh FLS1000 fluorescent spectrometer. On the device known as the UV-4600, the spectra of the diffuse reflection were examined., and the test errors were eliminated with the use of the reference provided by the $BaSO_4$ standard whiteboard.

3. Results and discussions

The XRD technique was applied to analyze the crystalline structure of the synthesized phosphor, and the results of the tests are presented in Figure 1(a). The figure typically comprised XRD spectra of BLSOF:0.15Tb^{3+}, BLSOF:0.15Tb^{3+},xSm^{3+} ($x = 0.12, 0.18, 0.24, 0.30$) , BLSOF:0.15Sm^{3+} phosphors and $Ba_2La_3(SiO_4)_3F$ (BLSOF) standard card (ICSD No.170852) was chosen to serve as the reference. There were no impurity peaks, and the intensity, number, and placement of the diffraction peaks were consistent with the typical card diffraction pattern. This illustrates that purity was absent in successfully producing the phosphors with an apatite structure. When Sm^{3+} and Tb^{3+} were introduced into the lattice replacing La^{3+}, it results in the formation of a single-phase solid solution compound.

Determining the optimum doping concentration of ion pairs for energy transfer is crucial for studying the impact of structural modulation of this process. According to the single variable method, the content of one doped rare earth ion needs to be fixed first, and the content of the other rare earth ions can change. In general, the content of the sensitizer can be fixed and the content of the activator can be changed during energy transfer. In the Tb^{3+}- Sm^{3+} double-doped phosphor studied in this paper, Tb^{3+} is used as a sensitizer, and Sm^{3+} is used as an activator. Therefore, for this system, it is necessary to fix the doping concentration of Tb^{3+} and change the doping concentration of Sm^{3+}. Therefore, to obtain a suitable Tb^{3+} doping concentration, we did a group of concentration intensity experiments on the BLSOF-doped Tb^{3+} phosphor. The relationship between rare earth doping concentration of BLSOF: yTb^{3+} phosphor and emission intensity of phosphor is depicted in Figure 1(b) and (c). Evidently, when the Tb^{3+} doping concentration is 0.15 mol, the luminous intensity reaches the maximum, and then the concentration quenching occurs, leading to the reduction of luminous intensity. In all subsequently co-doped phosphors, the concentration of Tb^{3+} could be fixed to 0.15 mol.

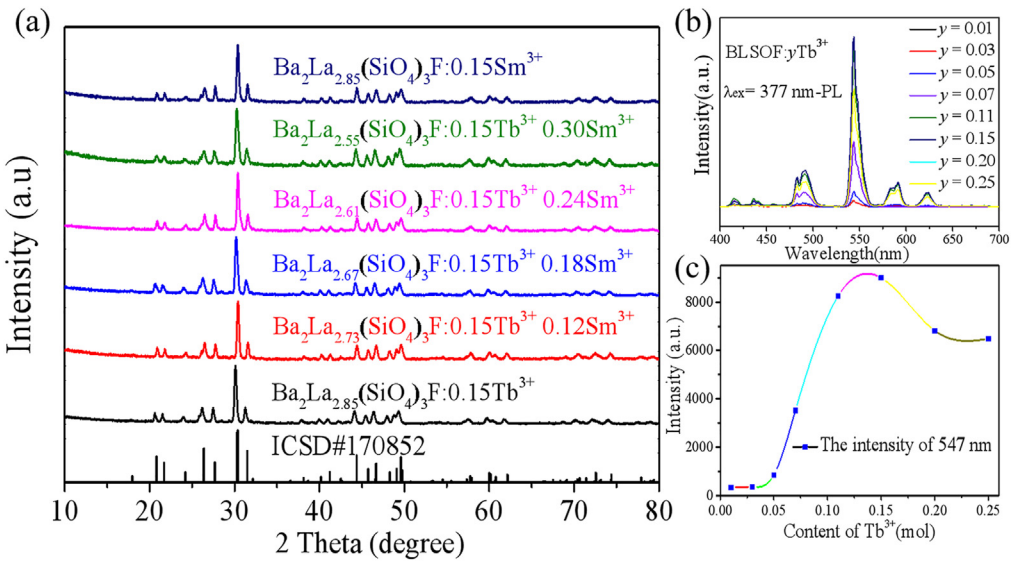

Figure 1. (a) BLSOF:Tb^{3+},Sm^{3+} samples' XRD patterns. For vivid comparison, the standard card for $Ba_2La_3(SiO_4)_3F$ (ICSD No.170852) is shown at the bottom. (b) The BLSOF:yTb^{3+} phosphors' emission spectra. (c) Relationship between BLSOF:yTb^{3+} phosphor concentration and intensity.

The Topas 3.0 tool was employed to optimize the phosphor structure to obtain crystallographic data. The Rietveld refinement-related preliminary data pertains to the BLSOF crystalline structure. A refinement was made to the Rietveld structure. Figure 2(a) provides a graphic representation of the findings that were generated. The computed strength is represented by solid lines in red, the measured strength is displayed by circles in blue, and the refined peak location of the Bragg diffraction is shown by short vertical lines in orange. A comparative analysis was done between the actual and estimated intensity, and the variation was displayed as a green solid line in the graph. Table 1 illustrates the outcomes of convergence that might be attained via refinement, together with lower R factors: $R_{exp} = 4.519\%$, $R_{wp} = 6.062\%$, $R_p = 4.515\%$, $\chi^2 = 1.342$. The parameters of the cell are as follows: a = b = 9.86354(36) **Å**, c = 7.36339(28) **Å,** and V = 620.402(51) **Å**^{3}. Table 2 contains the refined atomic coordinates that were obtained, and the BLSOF displays the isotropic temperature factors for each component atom.

A schematic representation of the BLSOF structure along the c-direction is displayed in Figure 2(b). La and Ba atoms each occupy two nonequivalent crystal positions within this structure, i.e. Ba1/La1 sites are placed at the *4f* position (C_3 point symmetry), whereas Ba2/La2 sites are situated at the *6h* position (C_S symmetry), each with nine and seven coordination, respectively. Silicon oxygen tetrahedron and fluorine ion are also marked in Figure 2(b).

BLSOF: 0.15Tb^{3+},0.16Sm^{3+}'s microcosmic state is depicted in Figure 3. The sample has an uneven and granular morphology when seen underneath a microscope, as portrayed in Figure 3(a). The energy distribution spectra peaks of Sm, Tb, F, O, Si, La, and Ba are shown by the EDS in Figure 3(b), which elaborate on the synthesis of the desired

Table 1. Data on the crystallography of BLSOF.

Formula	$Ba_2La_3(SiO_4)_3F$
Space group	$P6_3/m$
Symmetry	Hexagonal
a/b(Å)	9.86354(36)
c(Å)	7.36339(28)
a/b	90°
γ	120°
V(Å^3)	620.402(51)
R-Bragg	1.68801641
R_{exp}(%)	4.519
R_{wp}(%)	6.062
R_p(%)	4.515
χ^2	1.342

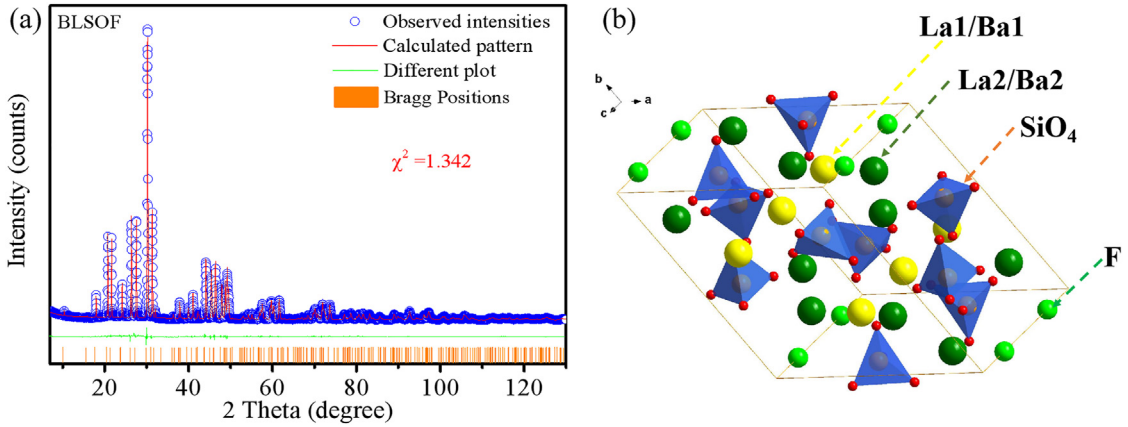

Figure 2. (a) $Ba_2La_3(SiO_4)_3F$'s Rietveld refinement XRD patterns generated by the TOPAS 3.0 software where the sample was held at room temperature. (b) The diagrammatic representation of the structure of the BLSOF along the c-direction.

Table 2. Atomic coordinates of BLSOF.

Atoms	Wyckoff	*x*	*y*	*z*	occ	beq
La2	6h	0.24004(26)	0.98731(37)	0.25	0.55	1
Ba2	6h	0.24004(26)	0.98731(37)	0.25	0.45	1
La1	4f	0.6666667	0.3333333	0.00011(79)	0.55	1
Ba1	4f	0.6666667	0.3333333	0.00011(79)	0.45	1
Si1	6h	0.40505(94)	0.36865(92)	0.25	1	1
O1	6h	0.5974	0.4496	0.25	1	1
O2	6h	0.3442	0.4996	0.25	1	1
O3	12i	0.356	0.2721	0.0751	1	1
F	2a	0	0	0.25	1	2.81

samples. Figure 3(c) provides a graphical depiction of element distribution, showing the microscopically even distribution of the synthetic sample.

Spectral analysis of the BLSOF phosphor's emission and excitation was performed. Afterwards, the BLSOF:0.15Tb^{3+} phosphors' PLE and PL spectra were recorded (Figure 4(a)). The normal excitation peaks of Tb^{3+} were seen in this PLE spectra approximately between 325 and 500 nm, whereas 377 nm was found to be the wavelength at which the emission peak had the highest strength value ($^7F_6 \rightarrow {}^5D_3$). When excited at a spectrum of 377 nm, the BLSOF: 0.15Tb^{3+} phosphor displayed a strong luminescence. The emission spectrum showed four primary emission peaks: 492 nm ($^5D_4 \rightarrow {}^7F_6$ transition), 547 nm ($^5D_4 \rightarrow {}^7F_5$ transition), 592 nm ($^5D_4 \rightarrow {}^7F_4$ transition), and 624 nm ($^5D_4 \rightarrow {}^7F_3$ transition), where 547 nm showed the strongest peak.

The outcomes of the research conducted on the excitation and emission wavelengths of the BLSOF:0.15Sm^{3+} phosphor are demonstrated in Figure 4(b). When triggered by a light with a wavelength of 405 nm, the BLSOF: 0.15Sm^{3+} phosphor exhibited a very strong luminosity. There were three main emission peaks shown in emission wavelength: 567, 603, and 651 nm with $^4G_{5/2} \rightarrow {}^6H_{J/2}$ (J = 5, 7, 9) transition. Figure 4(a) and 4(b) depict the overlap between the PLE (405 nm, 440 nm, and 474 nm) of Sm^{3+} and PL (492 nm) of Tb^{3+} are shown in slash, which could be explained theoretically as the transmission of energy from Tb^{3+} to Sm^{3+}.

Figure 4(c) displays the PL and PLE spectra of BLSOF:0.15Tb^{3+}, 0.16Sm^{3+} phosphor. Since the main focus of our study was to evaluate the transfer of energy from Tb^{3+} to Sm^{3+}, the excitation light of Tb^{3+} was chosen to excite the phosphor. Figure 4(c) provides a pink representation

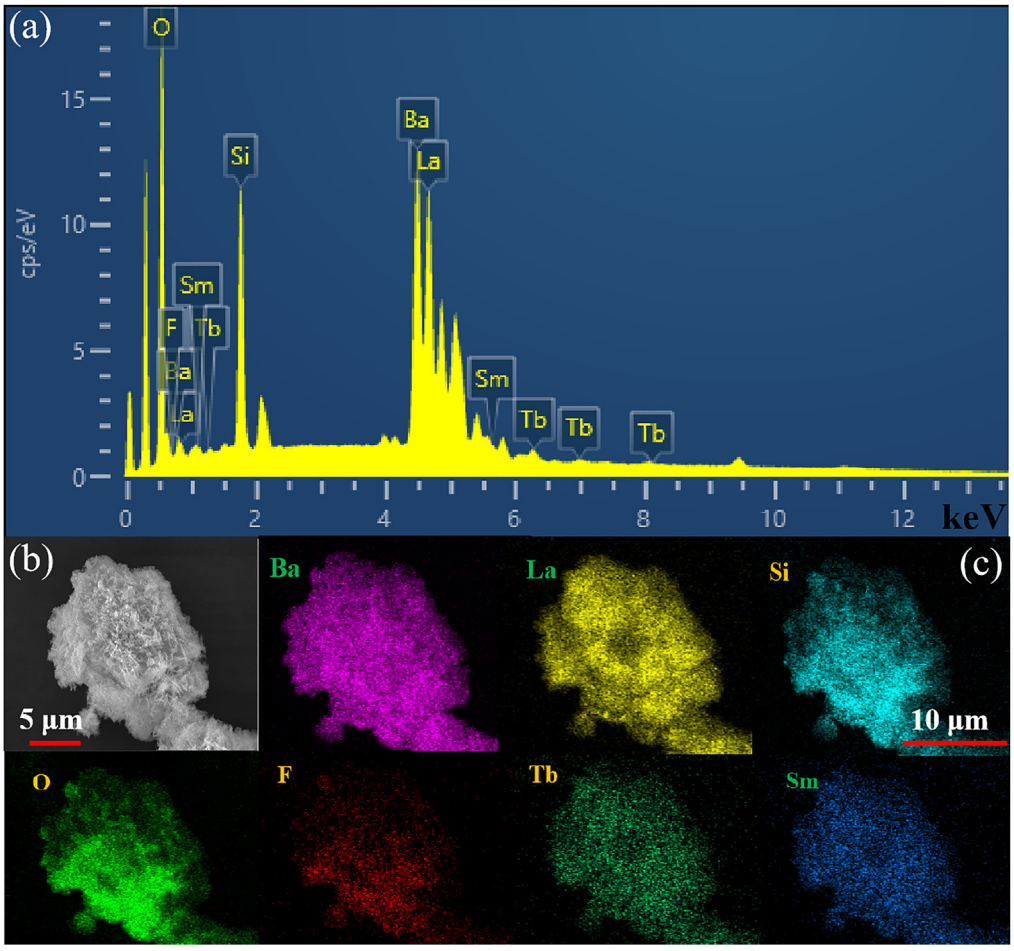

Figure 3. (a) EDS spectrum, (b) SEM image and (c) element mapping of BLSOF: 0.15Tb^{3+},0.16Sm^{3+}.

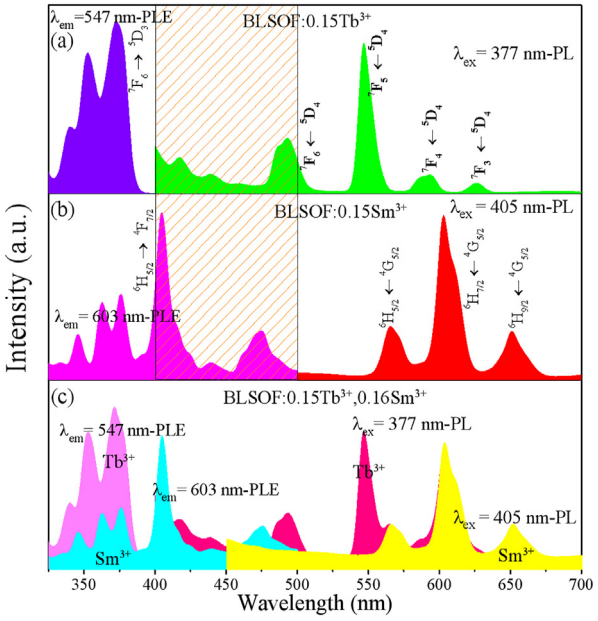

Figure 4. (a) Photoluminescence emission spectrum (right) and photoluminescence excitation spectrum (left) of BLSOF:0.15Tb^{3+} (b) Photoluminescence emission spectrum (right) and photoluminescence excitation spectrum (left) of BLSOF:0.15Sm^{3+} (c) Photoluminescence excitation spectrum (left) and photoluminescence emission spectrum (right) of BLSOF:0.15Tb^{3+}, 0.16Sm^{3+}.

of the PL spectrum obtained after phosphor activation at 377 nm. As expected, the wavelengths of samarium and the corresponding emissions of terbium were subjected to superposition. Both the distinctive emission peaks of Sm^{3+} (e.g. $^4G_{5/2}$-$^6H_{7/2}$ at 603 nm) and those of Tb^{3+}(e.g. $^5D_4$-$^7F_5$ at 547 nm) were observed in the emission wavelengths excited at 377 nm, establishing a firm groundwork for subsequent research on the colour refinement of this specific series of phosphors. Figure S1 contains a representation of the energy levels along with all of the related transitions to fully comprehend the mechanism of luminescence and the transfer of energy in a visualized manner.

After obtaining the spectrum of diffuse reflection, more research into the BLSOF optical band gap was conducted, as can be seen in Figure 5. Because BLSOF has a weak reflectivity in the UV region with wavelengths between 220-400 nm, it is deduced that it has a high absorption level in this region. As a result, it is possible to employ it as a substrate for luminous material-related energy absorption. Estimates of the BLSOF band gap Eg may be made using formula 1 [21, 22, 23]:

$$[h\nu F(R)]^2 = A(h\nu - Eg) \quad (1)$$

In line with Kubelka Munk formula 2 [24, 25]:

$$F(R) = \frac{(1-R)^2}{2R} = K \Big/ S \quad (2)$$

Where R stands for reflectivity, K denotes absorption, and S is for the scattering coefficient (1 can be taken here). When [hνF(R)] [2] = 0, the band gap of BLSOF can be derived using a linear model, approximated to 4.106 eV as illustrated in Figure 5. The wide band gap of BLSOF belongs to a semiconductor, which can accommodate various ions and their different excited states, is attractive for doping rare earth luminous ions and can serve as an appropriate substrate for luminescent materials.

The PL spectra of the BLSOF:0.15Tb3+,xSm3+(x = 0, 0.12, 0.16, 0.18, 0.20, 0.22, 0.24, 0.28, 0.30, 0.34) phosphors were displayed in Figure 6, where the signature spectra of Tb3+ (at 547 nm) and Sm3+ (at 603 nm) were further investigated. The general shape of each emission

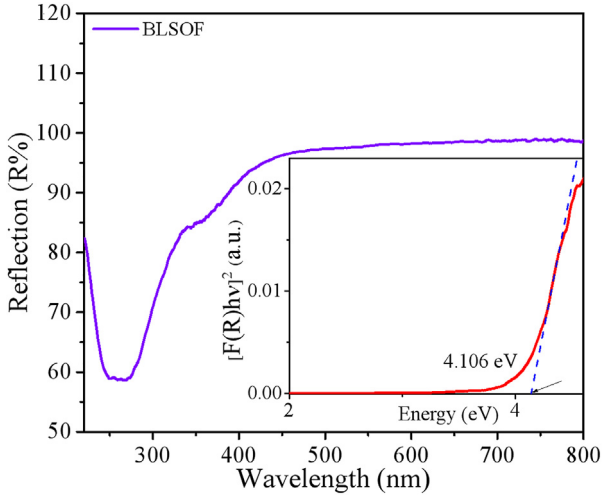

Figure 5. Diffuse reflection spectrum of BLSOF host and corresponding [F(R) hν] [2]-hν curve (inset) of as-obtained BLSOF sample.

spectrum is consistent, whereas the strength of the peak fluctuates in a predictable manner as the amount of doping with Sm3+ rises (Figure 6(a)). This fluctuation could be represented in Figure 6(b). Tb3+ to Sm3+ energy transfer may be responsible for the progressive decline in Tb3+ peak intensity. The initial rise in peak intensity of Sm3+ and the following weakening after reaching the highest point at 0.16 Sm3+ doping concentration, might be a result of the concentration quenching.

The Tb3+ emission lifetime of BLSOF: 0.15Tb3+,xSm3+, excited at 377 nm and observed at 547 nm, was studied to assess the mechanisms driving Tb3+→Sm3+ energy transfer (Figure 7(a)). The outcomes matched the estimates of formula 1 [20, 21]:

$$I(t) = I_0 + A_1 \exp(-t/\tau_1) + A_2 \exp(-t/\tau_2) \quad (1)$$

herein, I signify the PL intensity at time t, I_0 symbolizes the intensity at the start of the experiment, A_1 and A_2 symbolize the constants, t represents the time, and τ_1 and τ_2 denote the decay time following the energy-mediated excitation of the phosphor.

Formula 2 [22, 23] below provided the average lifetime:

$$\tau^* = \left(A_1\tau_1^2 + A_2\tau_2^2\right) / \left(A_1\tau_1 + A_2\tau_2\right) \quad (2)$$

The lifetimes of BLSOF:0.15Tb^{3+},xSm^{3+} (x = 0, 0.12, 0.16, 0.18, 0.20, 0.22, 0.24, 0.28, 0.30, 0.34) are obtained using the above formula, as listed in the legend of Figure 7(a). Notably, the lifetime of Tb^{3+} is reduced in the presence of a greater concentration of Sm^{3+}, which offered additional evidence that a transfer of energy had taken place in the BLSOF:0.15Tb^{3+},xSm^{3+} between the ions Tb^{3+} and Sm^{3+}.

The energy transfer efficiency in the BLSOF:0.15Tb^{3+},xSm^{3+} could be computed as per formula 3 [24, 25]:

$$\eta = 1 - (\tau_s / \tau_{s0}) \quad (3)$$

Herein, τ_{s0} is the value that indicates the luminescence intensity of the sensitizer Tb^{3+} when there is no Sm^{3+} present, and τ_s represents the luminescence intensity of Tb^{3+} when exposed to Sm^{3+}. η denotes the energy transfer efficiency in BLSOF:0.15Tb^{3+},xSm^{3+} calculated as a function of x, as portrayed in Figure 7(b).

Once the doping concentration of samarium in the BLSOF:0.15Tb^{3+},xSm^{3+} is gradually increased from 0.12, 0.16, 0.18, 0.20, 0.22, 0.28, 0.30–0.34 mol, the energy transfer efficiency is calculated to be 27.05%, 33.43%, 39.11%, 42.54%, 45.01%, 45.44%, 50.76%, and 60.00%, respectively (Figure 7(b)). Notably, raising the doping concentration of the samarium contributed to a greater energy transfer efficiency.

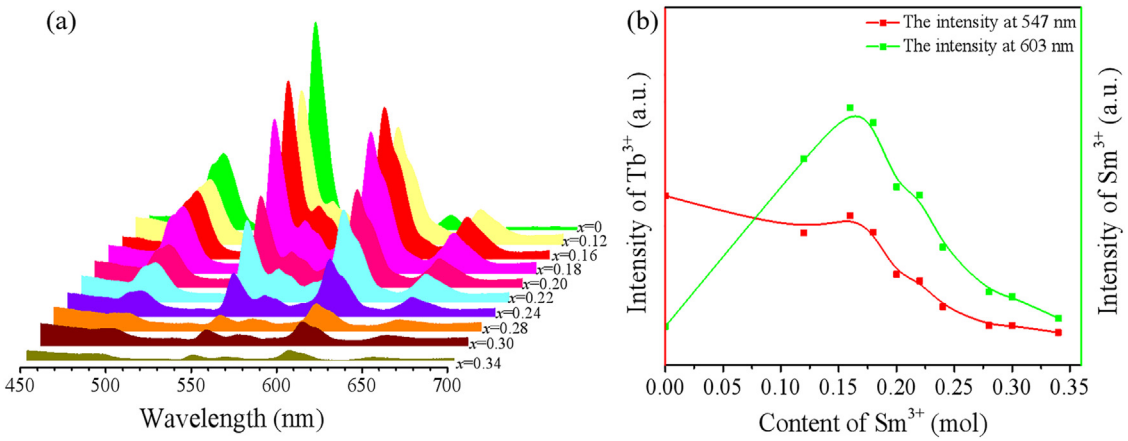

Figure 6. (a) The PL spectra of the BLSOF:0.15Tb3+,xSm3+(x = 0, 0.12, 0.16, 0.18, 0.20, 0.22, 0.24, 0.28, 0.30, 0.34) phosphors (b) The PL intensities of 547 nm (Tb3+) and 603 nm (Sm3+) when excited by 377 nm with the increase of Sm3+ contents (x).

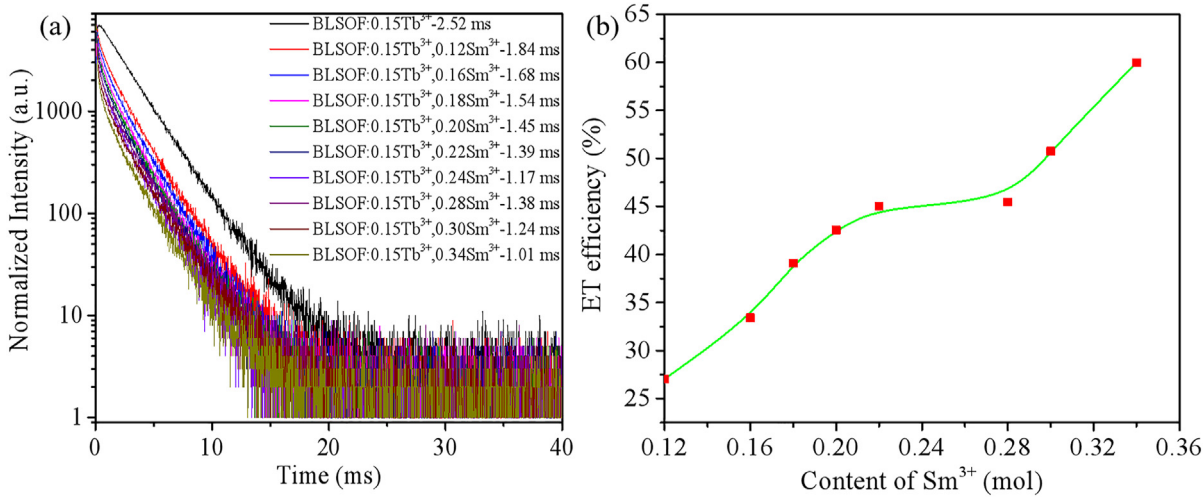

Figure 7. (a)The fluorescence decay spectrum of BLSOF:0.15Tb^{3+},xSm^{3+}. The wavelength of 377 nm is used for excitation, while 547 nm is used for monitoring. (b) The energy transfer efficiency of the phosphor under different contents of Sm^{3+}.

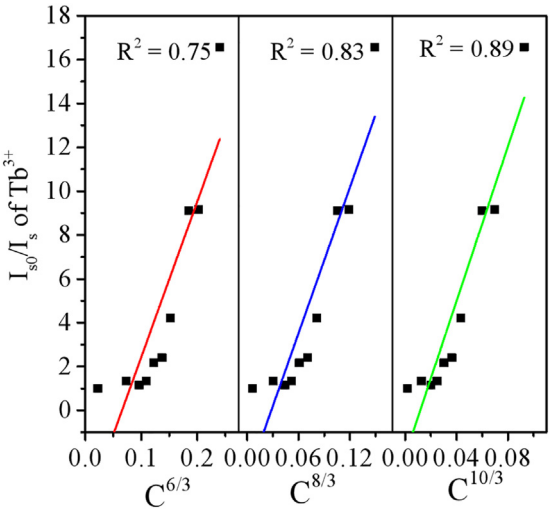

Figure 8. The relationship between I_{S0}/I_S of Tb^{3+} in BLSOF and $C^{6/3}$, $C^{8/3}$ and $C^{10/3}$.

The non-radiative transfer of energy may occur as a result of either the exchange interplay or the electric dipole interplay between the activators and the sensitizers, or between the activators themselves. A wide variety of non-radiative transmissions of energy may be categorized via critical distance analysis. Formula 4 below can be used to calculate the critical distance Rc in compliance with the BLASSE theory [26, 27, 28]:

Table 3. CIE coordinate values of BLSOF:0.15Tb^{3+}, xSm^{3+} at different Sm^{3+} doping concentrations.

Formula	CIE Value
$Ba_2La_{2.85}(SiO_4)_3F$:0.15Tb^{3+}	(0.3672,0.6111)
$Ba_2La_{2.73}(SiO_4)_3F$:0.15Tb^{3+}, 0.12Sm^{3+}	(0.4663,0.5185)
$Ba_2La_{2.69}(SiO_4)_3F$:0.15Tb^{3+}, 0.16Sm^{3+}	(0.4754,0.5115)
$Ba_2La_{2.67}(SiO_4)_3F$:0.15Tb^{3+}, 0.18Sm^{3+}	(0.4748,0.5105)
$Ba_2La_{2.65}(SiO_4)_3F$:0.15Tb^{3+}, 0.20Sm^{3+}	(0.4770,0.5072)
$Ba_2La_{2.63}(SiO_4)_3F$:0.15Tb^{3+}, 0.22Sm^{3+}	(0.4788,0.5051)
$Ba_2La_{2.61}(SiO_4)_3F$:0.15Tb^{3+}, 0.24Sm^{3+}	(0.4748,0.5065)
$Ba_2La_{2.57}(SiO_4)_3F$:0.15Sm^{3+}, 0.28Sm^{3+}	(0.4617,0.5142)
$Ba_2La_{2.55}(SiO_4)_3F$:0.15Tb^{3+}, 0.30Sm^{3+}	(0.4586,0.5171)
$Ba_2La_{2.51}(SiO_4)_3F$:0.15Tb^{3+}, 0.34Sm^{3+}	(0.4581,0.5174)
$Ba_2La_{2.85}(SiO_4)_3F$:0.15Sm^{3+}	(0.5783,0.4168)

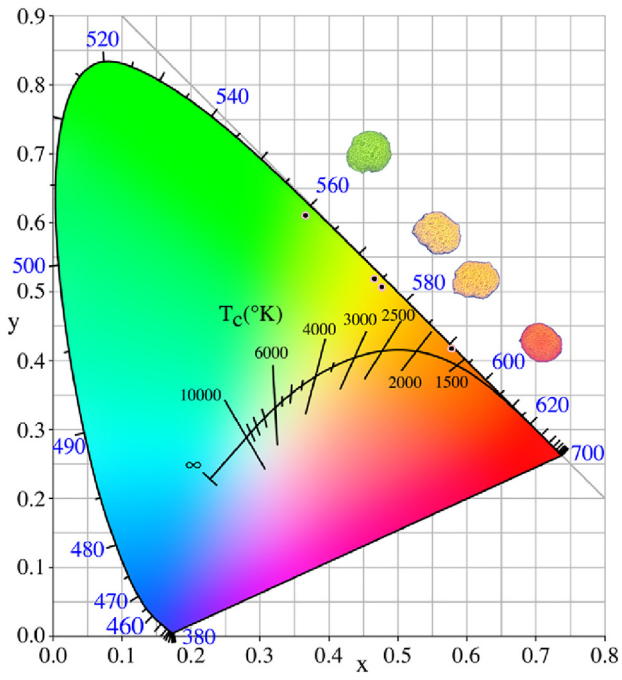

Figure 9. CIE of BLSOF:0.15Tb^{3+}, *x*Sm^{3+} when excited by 377 nm.

$$R_c \approx 2(3V/4\pi x_c N)^{1/3} \quad (4)$$

herein, the volume of a unit cell is symbolized by V, samarium and terbium's total concentration is denoted by the symbol x_c when the energy efficacy is set to 0.5, and the parameter of N indicates the number of cations present for a single unit cell. For $Ba_2La_3(SiO_4)_3F$ host, N = 10 and V = 608.8 Å [**3**]. As displayed in Figure 7(b), when the energy transfer efficiency is at a value of 0.5, the Sm^{3+} doping concentration is approximately 0.3 mol. Therefore, $x_c = 0.3 + 0.15 = 0.45$ mol. According to the findings of the computation, the value of Rc for BLSOF:0.15Tb^{3+}, *x*Sm^{3+} is approximately 0.637032 nm. Since the critical distance for the BLSOF:0.15Tb^{3+}, *x*Sm^{3+} is >0.5 nm, electric dipole interactions serve as the mode of *x*Sm^{3+} for transferring energy.

There are three distinct categories of interactions between electric dipoles: dipole-dipole, dipole-quadrupole, and quadrupole-quadrupole interactions. Applying formula 5 below further substantiates the mode of transferring energy [29, 30, 31, 32]:

$$(I_{s0} / I_s) \propto C^{n/3} \quad (5)$$

Herein, I_{S0} symbolizes the PL intensity of Tb^{3+} in BLSOF:0.15Tb^{3+} phosphor; I_S highlights the PL intensity of Tb^{3+} in BLSOF:0.15Tb^{3+},*x*Sm^{3+} phosphor; C represents the total concentration of terbium and samarium; *n* symbolizes the constant, which can be used to explain how samarium and terbium exchange energy with one another. The energy transfer occurs through dipole-dipole, dipole-quadrupole, and quadrupole-quadrupole interactions for n = 6, 8, and 10, correspondingly. Figure 8 demonstrates that the optimum linear fitting I_{S0}/I_S and $C^{n/3}$ (n = 6, 8, or 10) when n is 10, suggesting that the energy transfer mechanism underpinning BLSOF:0.15Tb^{3+},*x*Sm^{3+} is the quadrupole-quadrupole interface.

Table 3 provides the outcomes of the analysis of the BLSOF:0.15Tb^{3+},*x*Sm^{3+} phosphor's emission spectra, which helped determine its colour coordinates. These colour coordinates have been highlighted on the CIE diagram so that the phosphor colour alteration may be more prominent (Figure 9). Evidently, the modification of the ratio of Tb^{3+} to Sm^{3+} in the doping concentrations contributed to a shift in the phosphor colour from green (0.37, 0.61) to yellow and reddish colour (0.58, 0.42). The series of phosphors that are produced when they are exposed to irradiation from a 365 nm miner's lamp at samarium doping concentrations of 0, 0.12, and 0.20 mol of BLSOF:0.15Tb^{3+},*x*Sm^{3+}, and BLSOF:0.15Sm^{3+}, correspondingly, are shown in the images that are located from top to bottom in Figure 9. Overall, this set of new single-phase phosphors, known as BLSOF:0.15Tb^{3+}, *x*Sm [3], displays the significance of configurable polychromatic luminescence owing to energy transfer.

4. Conclusions

Single-phase polychromatic phosphor BLSOF:0.15Tb^{3+},*x*Sm^{3+} was synthesized using the commonly used high-temperature solid phase method. Extensive research has been conducted to investigate both the structure and the optical characteristics of this phosphor. We concluded based on our analysis that the optimum concentration of Sm^{3+} to employ in BLSOF:0.15Tb^{3+},*x*Sm^{3+} is 0.16 mol. In BLSOF, it was discovered that the mode of energy transfer from Tb^{3+} to Sm^{3+} occurs via the quadrupole-quadrupole (q-q) interplay. Based on the amounts of Tb^{3+}/Sm^{3+} that are doped into the phosphors, the colour of the phosphors may change from green to yellow to reddish colour. Overall, BLSOF:0.15Tb^{3+},*x*Sm^{3+} may act as an excellent single-phase multicolour phosphor.

Declarations

Author contribution statement

Kun Nie: Conceived and designed the experiments; Wrote the paper.

Ranan Zhou: Performed the experiments.

Chi-An Cheng, Lefu Mei, Haikun Liu, Yuanyuan Zhang, Luoxin Wang, Hua Wang: Analyzed and interpreted the data.

Xiuqiang Duan, Ziyao Hu: Contributed reagents, materials, analysis tools or data.

Xiaoxue Ma: Conceived and designed the experiments; analyzed and interpreted the data.

Funding statement

Lefu Mei was supported by National Natural Science Foundation of China [51872269], National Natural Science Foundation of China [52274273].

Dr. Kun Nie was supported by the Science and Technology Research Project of Hubei Provincial Department of Education [B2021091], Key Laboratory for New Textile Materials and Applications of Hubei Province(Wuhan Textile University) [FZXCL202107], Key Laboratory of Testing and Tracing of Rare Earth Products for State Market Regulation (Jiangxi University of Science and Technology) [TTRE-P2022YB04].Haikun Liu was supported by Basic and Applied Basic Reuter Foundation of Guangdong Province [2021A1515110702].Yuanyuan Zhang was supported by Basic and Applied Basic Reuter Foundation of Guangdong Province [2021A1515110283], China Postdoctoral Science Foundation [2021M702562].

Data availability statement

Data will be made available on request.

Declaration of interests statement

The authors declare no conflict of interest.

Additional information

Supplementary content related to this article has been published online at https://doi.org/10.1016/j.heliyon.2022.e12566.

Acknowledgements

This research was supported by Key Laboratory of Testing and Tracing of Rare Earth Products for State Market Regulation (Jiangxi University of Science and Technology) (TTREP2022YB04), the National Natural Science Foundation of China (51872269, 52274273), the Science and Technology Research Project of Hubei Provincial Department of Education (B2021091), Key Laboratory for New Textile Materials and Applications of Hubei Province(Wuhan Textile University) (FZXCL202107), the Open Project Program of High-Tech Organic Fibers Key Laboratory of Sichuan Province and National Project Cultivation Plan of Wuhan Textile University. The authors would like to thank Liu Nian and Liu Tianying from Shiyanjia Lab (www.shiyanjia.com) for the XRD, and SEM characterizations. We sincerely thank Prof. Dr. Chi-An Cheng from National Taiwan University, for polishing the paper. This work was partially financially supported by Guangdong Basic and Applied Basic Reuter Foundation (2021A1515110283 and 2021A1515110702), the Project funded by China Postdoctoral Science Foundation (2021M702562).

References

[1] B. Demir, E. Ayas, Effects of sintering temperature and doping content on luminescence properties of rare earth (Sm^{+3}, Eu^{3+}, and Dy^{3+}) doped natural fluorapatite, J. Solid State Chem. 306 (2022) 122783.

[2] K. Nie, X. Ma, P. Lin, N. Kumar, L. Wang, L. Mei, Synthesis and luminescence properties of apatite-type red-emitting $Ba_2La_8(GeO_4)_6O_2:Eu^{3+}$ phosphors, J. Rare Earth. 39 (2021) 1320–1326.

[3] H. Qian, C. Fan, F. Hussain, K. Song, X. Luo, W. Su, H. Wang, Q. Huang, L. Yang, Energy transfer between two luminescent centers and photoluminescent properties of $Ca_{4-y}La_6(AlO_4)_x(SiO_4)_{6-x}O_{1-x/2}$: yEu^{2+} apatite structure phosphors, J. Lumin. 235 (2021) 117991.

[4] H. Liu, L. Mei, L. Liao, Y. Zhang, Q. Guo, T. Zhou, Y. Wang, L. Li, Strategy for realizing ratiometric optical thermometry via efficient Tb^{3+}-Mn^{2+} energy transfer in novel apatite-type phosphor $Ca_9Tb(PO_4)_5(SiO_4)F_2$, J. Alloy. Compd. 770 (2019) 1237–1243.

[5] B. Demir, D. Derince, T. Dayioglu, L. Koroglu, E. Karacaoglu, V. Uz, E. Ayas, Effects of doping content and crystallite size on luminescence properties of Eu^{3+} doped fluorapatites obtained from natural waste, Ceram. Int. 47 (2021) 34657–34666.

[6] W. Yan, J. Li, W. Zhang, X. Gao, P. Zhang, Warm-white luminescence of Dy^{3+} and Sm^{3+} co-doped $NaSrPO_4$ phosphors through energy transfer between rare earth ions, J. Mater. Sci.-Mater. El. 32 (2021) 16648–16661.

[7] P. Dang, G. Li, S. Liang, H. Lian, J. Lin, Multichannel photoluminescence tuning in Eu-doped apatite phosphors via coexisting cation substitution, energy transfer and valence mixing, J. Mater. Chem. C 7 (2019) 5975–5987.

[8] H. Liu, L. Liao, S.M. Aksenov, Q. Guo, L. Mei, D.V. Deyneko, Novel Dy^{3+}-doped Ge^{4+}-substituted apatite-type phosphors, $Ca_9La(PO_4)_5[(Si_{1-x}Ge_xO4)]F_2:Dy^{3+}$: Synthesis, structure, crystal chemical features, and luminescent properties, Ceram. Int. 47 (2021) 23300–23308.

[9] T. Tian, W. Liu, Q. Liu, Y. Zhang, Y. Chu, G. Liu, J. Xu, A new oxyapatite red phosphor Eu^{3+}-doped $Ca_3Y_7(BO_4)(SiO_4)_5O$: Synthesis, structure and luminescence properties, J. Rare Earth. 40 (2022) 709–716.

[10] S. Slimi, P. Loiko, K. Bogdanov, A. Volokitina, R.M. Solé, M. Aguiló, F. Díaz, E. Ben Salem, X. Mateos, Structure and luminescent properties of Dy^{3+} activated $NaLa_9(SiO_4)_6O_2$ yellow-emitting phosphors for application in white LEDs, J. Alloy. Compd. 896 (2022) 163109.

[11] N. Baig, R.S. Yadav, N.S. Dhoble, V.L. Barai, S.J. Dhoble, Near UV excited multi-color photoluminescence in RE^{3+} (RE=Tb, Sm, Dy and Eu) doped $Ca_2Pb_3(PO_4)_3Cl$ phosphors, J. Lumin. 215 (2019) 116645.

[12] I. Jeon Yong, L. Krishna Bharat, J.S. Yu, White-light emission of $Ca_2La_8(GeO_4)_6O_2$: Tb^{3+}/Sm^{3+} nanocrystalline phosphors for solid-state lighting applications, J. Lumin. 166 (2015) 93–100.

[13] K. Su, Q. Guo, P. Shuai, M. Xiang, G. Zhang, Z. Yan, L. Mei, L. Liao, High thermal stability pyroxene type $CaScAlSiO_6:Tb^{3+}/Sm^{3+}$ ceramics with excellent cryogenic optical thermometry performance, Ceram. Int. 48 (2022) 4675–4685.

[14] L. Dong, L. Zhang, Y. Jia, B. Shao, W. Lü, S. Zhao, H. You, Synthesis, luminescence and application of novel europium, cerium and terbium-doped apatite phosphors, CrystEngComm 21 (2019) 6226–6237.

[15] Y. Zhang, J. Bin, L. Mei, Z. Huang, Synthesis and luminescence properties of reddish orthosilicate oxyapatite phosphor $LiGd_9(SiO_4)_6O_2:Sm^{3+}$, J Lumin 206 (2019) 645–648.

[16] H. Ye, M. He, T. Zhou, Q. Guo, J. Zhang, L. Liao, L. Mei, H. Liu, M. Runowski, A novel reddish-orange fluorapatite phosphor, $La_{6-x}Ba_4(SiO_4)_6F_2$: xSm^{3+} - Structure, luminescence and energy transfer properties, J. Alloy. Compd. 757 (2018) 79–86.

[17] H. Liu, L. Liao, D. Yang, Q. Guo, L. Mei, Synthesis, photoluminescence properties and energy transfer behavior of color-tunable fluorapatite phosphor $Sr_9Gd(PO_4)_5(SiO_4)F_2:Tb^{3+}/Sm^{3+}$, Ceram. Int. 42 (2016) 16579–16583.

[18] X. Ma, L. Liao, Q. Guo, H. Liu, T. Zhou, L. Mei, Luminescence properties and energy transfer investigations of $Ba_2La_{2.85-x}Tb_{0.15}Eux(SiO_4)_3F$ multicolor phosphor, RSC Adv 8 (2018) 27332–27341.

[19] Q. Guo, X. Ma, L. Liao, H. Liu, D. Yang, N. Liu, L. Mei, Structure and luminescence properties of multicolor phosphor $Ba_2La_3(SiO_4)_3Cl:Tb^{3+},Eu^{3+}$, J. Solid State Chem. 280 (2019) 121009.

[20] H. Liu, K. Nie, Y. Zhang, L. Mei, D.V. Deyneko, X. Ma, J. Rare Earth. (2022).

[21] Y. Wu, Y. Zhuang, Y. Lv, K. Ruan, R.-J. Xie, A high-performance non-rare-earth deep-red-emitting $Ca_{14-x}Sr_xZn_6Al_{10}O_{35}:Mn^{4+}$ phosphor for high-power plant growth LEDs, J. Alloy. Compd. 781 (2019) 702–709.

[22] J. Tauc, Optical properties and electronic structure of amorphous Ge and Si, Mater. Res. Bull. 3 (1968) 37–46.

[23] T.M. Tolhurst, T.D. Boyko, P. Pust, N.W. Johnson, W. Schnick, A. Moewes, Investigations of the Electronic Structure and Bandgap of the Next-Generation LED-Phosphor $Sr[LiAl_3N_4]:Eu^{2+}$—Experiment and Calculations, Adv. Opt. Mater. 3 (2015) 546–550.

[24] D. Xu, W. Zhou, Z. Zhang, X. Ma, Z. Xia, Luminescence property and energy transfer behavior of apatite-type $Ca_4La_6(SiO_4)_4(PO_4)_2O_2:Tb^{3+}$, Eu^{3+} phosphor, Mater. Res. Bull. 108 (2018) 101–105.

[25] S. Yan, Y. Jin, D. Pan, G. Xiang, X. Luo, Y. Yang, $Sr_4Y_6(AlO_4)x(SiO_4)_{6-x}O_8:Eu^{2+}$: A novel apatite structure blue-green emitting phosphor, Ceram. Int. 44 (2018) 19900–19906.

[26] K. Nie, R. Zhou, C.-A. Cheng, X. Duan, Z. Hu, L. Mei, H. Liu, L. Wang, H. Wang, X. Ma, Tb^{3+} and Sm^{3+} co-doped $Ca_2La_3(SiO_4)_3F$ phosphor: synthesis, color regulation, and luminescence properties, RSC Adv 12 (2022) 33200–33206.

[27] X.X. Ma, W. Zhou, Z. Zhang, X.R. Wang, B. Zhang, Y.-C. Guo, Preparation and luminescence properties of $Ba_3LaNa(PO_4)_3F:Ce^{3+},Tb^{3+}$ phosphors, J. Lumin. 199 (2018) 82–86.

[28] Y. Jin, Y. Wang, Y. Wang, Tuning luminescence and excellent thermal stability of $Gd_{4.67}Si_3O_{13}$: Bi^{3+}, Eu^{3+} with energy transfer from Bi^{3+} to Eu^{3+}, Ceram. Int. 46 (2020) 22927–22933.

[29] X. Ma, L. Liao, Q. Guo, H. Liu, D. Yang, N. Liu, L. Mei, Structure and luminescence properties of multicolor phosphor $Ba_2La_3(GeO_4)_3F:Tb^{3+},Eu^{3+}$, RSC Adv 9 (2019) 35717–35726.

[30] Y. Zhao, S. Wang, Y.-j. Han, J.-y. Zhang, C. Liu, X.-f. Hu, Z.-w. Zhang, L.-j. Wang, Luminescence properties and energy transfer in Ce^{3+} and Tb^{3+} co-doped $Sr_5(PO_4)_2SiO_4$ phosphor, J. Lumin. 223 (2020) 117253.

[31] R. Zhou, C.-A. Cheng, S. Qiu, J. Chen, K. Nie, M. Wu, P. Lin, H. Wang, L. Wang, L. Mei, A novel and facile synthesis strategy for highly stable cesium lead halide nanowires, RSC Adv 11 (2021) 28716–28722.

[32] Y. Ma, X. Peng, M. Fei, W. Zhang, L. Teng, F. Hu, R. Wei, H. Guo, Adjustable white luminescence and high thermal stability in $Eu^{2+}/Eu^{3+}/Tb^{3+}$/Al co-doped aluminosilicate oxyfluoride glass, J. Alloy. Compd. 846 (2020) 156435.